High-resolution single pulse LA-ICP-MS mapping via 2D sub-pixel oversampling on orthogonal and hexagonal ablation grids – A computational assessment

Dino Metarapi, Johannes T. van Elteren [*]

Department of Analytical Chemistry, National Institute of Chemistry, Hajdrihova 19, 1000, Ljubljana, Slovenia

A B S T R A C T

Laser beam profiles in analytical laser ablation – inductively coupled plasma – mass spectrometry (LA-ICP-MS) instruments are in general homogenized to produce a flat-top beam profile. However, in practice, they are mostly super-Gaussian in nature, and for small laser beam sizes (<5 μm) they even approach a Gaussian profile. This implies that the amount of surface material sampled by the laser (=ablation volume) directly depends on the beam profile and ablation grid. By contraction of the ablation grid (=sub-pixel mapping) not only more accurate surface sampling is realized, but also a higher pixel density, an improved spatial resolution, and a better signal-to-noise ratio. Although LA sampling is predominantly performed on an orthogonal grid, hexagonal or staggered/interleaved sampling may further improve the image quality as regular hexagons are more compact than squares (=lower perimeter/area) and suffer less from orientation bias (=lower anisotropy). Due to the current limitations of LA stages in executing precise hexagonal sampling with small beam sizes, computational protocols were employed to simulate LA-ICP-MS mapping. Simulation was performed by discrete convolution using the crater profile as the kernel, followed by the application/addition of Poisson/Flicker noise related to the local concentration and instrumental sensitivity/noise. A freely accessible online app was developed (https://laicpms-apps.ki.si/webapps/home/) to study the effect of sampling grid contraction (orthogonal and hexagonal) on the image map quality (spatial resolution and signal-to-noise ratio) by virtual ablation of phantoms. Comparison of experimental LA-ICP-MS maps obtained through orthogonal and hexagonal sampling methods could only be performed using a beam size of 150 μm and a macroscale inkjet-printed resolution target. This was due to the unavailability of precise hexagonal sampling stages and microscale resolution targets, which prevented the use of smaller beam sizes.

1. Introduction

In recent years we have witnessed a surge of improvements in LA-ICP-MS mapping which have had a profound effect on mapping speed and spatial resolution. The single largest improvement can be attributed to the development of LA cells for fast washout of aerosol particles, combined with interfaces with negligible dispersion [1–3]. As a result, LA-ICP-MS mapping in single pulse mode has seen pixel acquisition rates approaching or exceeding 1 kHz [4,5]. Such acquisition rates, in combination with sensitive ICP-MS instrumentation, allow for the sampling of large surfaces with small laser beam sizes (<10 μm). In many bio-applications, "thin" samples can be prepared so that a single laser shot already removes all the material in the ablation spot [6,7], implying that

by partially overlapping ablation spots the spatial resolution can be increased. However, sensitivity issues and concomitant noise may start to play a role at low concentration levels, small beam sizes, and/or insufficiently sensitive detectors [8].

To overcome such sensitivity issues in LA-ICP-MS, we are strong proponents of 1D-oversampling strategies by line scanning of "thick" samples so that the counts of multiple partially overlapping laser shots (=dosage) are accumulated to generate a single pixel [9]. However, the latest generation of fast response cells (washout time <10 ms) [2] may max out the repetition rate in this mode for the same scanning speed [10]. A washout time of say 5 ms (=FW0.01 M, full width at 1% maximum) requires a repetition rate of 2000 Hz at a dosage of 10, to fulfill the multiple oversampling criteria and avoid aliasing in

multielement mapping [11,12], thereby practically limiting the use of such fast response cells in 1D-oversampling mode for ultrafast mapping. The conventional single pulse mode (dosage = 1) can cope much better with such fast response cells as ten times fewer pulses are required in the same time interval, thereby allowing much higher scanning speeds and thus mapping times. Multielement imaging in this mode is preferably performed by simultaneous ICP-TOFMS instruments as sequentially scanning quadrupole detectors can generally measure only a single element in the timeframe associated with the washout of a single pulse in the fastest response cells due to hopping and settling times [13].

However, as fewer counts are accumulated per pixel in single pulse mode than in 1D-oversampling mode, we will investigate how 2D-over-sampling of ablation spots in orthogonal and hexagonal fashion may aid in generating a better quality LA-ICP-MS map than conventional spot-resolved mapping. Published research on orthogonal ablation grids has shown that this oversampling technique has the potential for increasing the image quality of low-concentration samples, both for mapping with MALDI [14] and LA-ICP-MS [8]. In general, 2D over-sampling leads to a higher pixel density and images with less noise and more detail. It is important to realize that the beam profile is of critical importance for surface sampling as ablation on a conventional single pulse ablation grid (=orthogonal) may technically undersample the surface, leaving a dimpled topography. More dense packing of ablation spots (by contracting the ablation grid) increases the pixel density, and thus the spatial resolution, for a more accurate assessment of the actual elemental surface distribution. Van Malderen et al. [15] already demonstrated that after contraction of an orthogonal grid the near Gaussian-type crater geometries produced by a 3-μm round ablation spot yielded a smooth post-ablation surface.

Although unusual, and prone to complicate matters associated with laser sampling and data processing, sampling on a hexagonal grid may enhance the image quality in single pulse LA-ICP-MS mapping even further as hexagonal pixels or hexagons are more compact than squares, whereas also edge artifacts are reduced [16]. Furthermore, the perceived visual image quality may improve as high-density cones in the retina are also placed and shaped in a hexagonal arrangement [16–18]. Simulation via virtual LA-ICP-MS mapping of phantoms (high-resolution image, chirp resolution target, and contrast-detail diagram) will show the performance characteristics of orthogonal and hexagonal sampling of the surface, next to gaining insights into spatial resolution and the effect of noise on the loss of detail. To this end, an online app was developed based on discrete convolution with point spread functions associated with the crater profile, in combination with the introduction of Flicker and Poisson noise as representative sources of instrumental noise and counting statistics, respectively. An experimental confirmation of the benefits of hexagonal sampling was obtained using a large beam size (150 μm) as accurate sampling with generic orthogonal stages becomes less critical. To this end an inkjet-printed chirp resolution target [19] was subjected to LA-ICP-MS mapping by measuring the Cu distribution in the cyan ink [20].

2. Computational methodologies

2.1. LA sampling and crater geometry

Laser ablation crater geometries associated with square or round beam profiles are rarely defined by a true square cuboid or cylinder as in practice a spatially coherent energy density obtained by beam shaping resembles at best a symmetric probability density function with high super-Gaussian order. Square and round super-Gaussian beam profiles deliver their focused, pulsed energy to a material, leading to typical ablation crater geometries as a function of the material's optical properties and their interaction with the laser light wavelength. Super-Gaussian beam profiles can be described by the following equations (for round (○) and square (□) beam profiles):

$$F(○) = F_p \times \exp[-2 \times (r/\omega_0)^n] \tag{1}$$

and

$$F(□) = F_p \times \exp[(-2 \times |x|^n - 2 \times |y|^n)/\omega_0^n] \tag{2}$$

where $F(○)$ and $F(□)$ are associated with the round and square fluence distribution in the ablation spot, respectively, with r and (x,y) denoting the radial distance and orthogonal coordinates, and n representing the order of the super-Gaussian probability density function. The focused beam, defined as the distance from the center of the ablation spot to the edge where the fluence equals $1/e^2$ times the peak fluence F_p, ablates the material above a certain threshold fluence F_{th}.

The maximum ablation depth D_{max} per shot (in μm) increases logarithmically with the peak fluence F_p according to the following equation [21]:

$$D_{max} = (1/\propto) \times \ln(F_p/F_{th}) \tag{3}$$

where α is the spectral absorption coefficient. Fig. 1 shows how the laser ablation spots, and the associated ablation craters, are directly linked to the super-Gaussian order n. The ablation craters produced by normal Gaussian beam profiles for round and square profiles are identical as Eqs. (1) and (2) convert to the same fluence distribution at $n = 2$. The presence of less steep edge transitions in beam profiles with lower Gaussian order, visible from the red trace representing the profiles through the middle of the ablation craters in Fig. 1, leads to a less efficient delivery of energy and a greater heat-affected zone which may negatively affect damage to the area surrounding the ablation spot [22]. However, due to the short pulse duration, usually in the ns (or lower) range, unwanted surface degradation due to surplus heating phenomena can be greatly reduced. Nevertheless, analytical LA devices are preferably tuned to have a flat-top beam profile, although for beam sizes <5 μm the beam profile by definition approaches a normal Gaussian profile due to diffraction.

2.2. 2D sampling on contracted orthogonal and hexagonal ablation grids

Although a true square cuboid beam profile would be ideal for perfect surface sampling, in practice we usually deal with round super-Gaussian beam profiles, especially due to their availability in the small beam size range and the fact that square beam profiles in that range would tend to be round(ed) anyway. However, round beam profiles may seriously undersample the surface, depending on the beam profile morphology and ablation grid layout, as shown in Fig. 2. It is evident
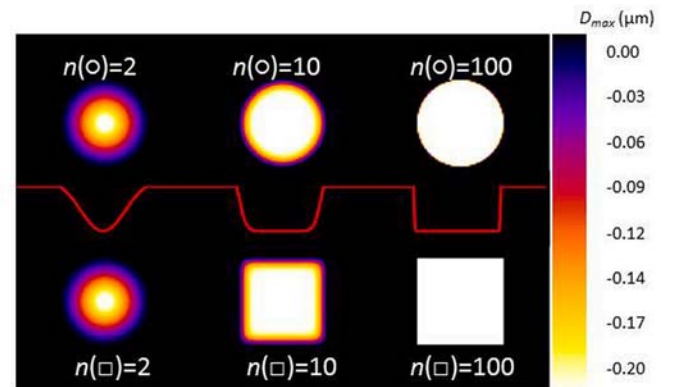

Fig. 1. Theoretical crater geometry generated upon single shot laser ablation for similarly sized square (□) and round (○) beam profiles with super-Gaussian orders n of 2, 10, and 100. The maximum ablation depth D_{max} is based on real-life values for the spectral absorption coefficient α (0.0134 nm^{-1}), threshold fluence F_{th} (0.263 J cm^{-2}), and peak fluence F_P (4 J cm^{-2}), all associated with ablation of borosilicate glass at 193 nm.
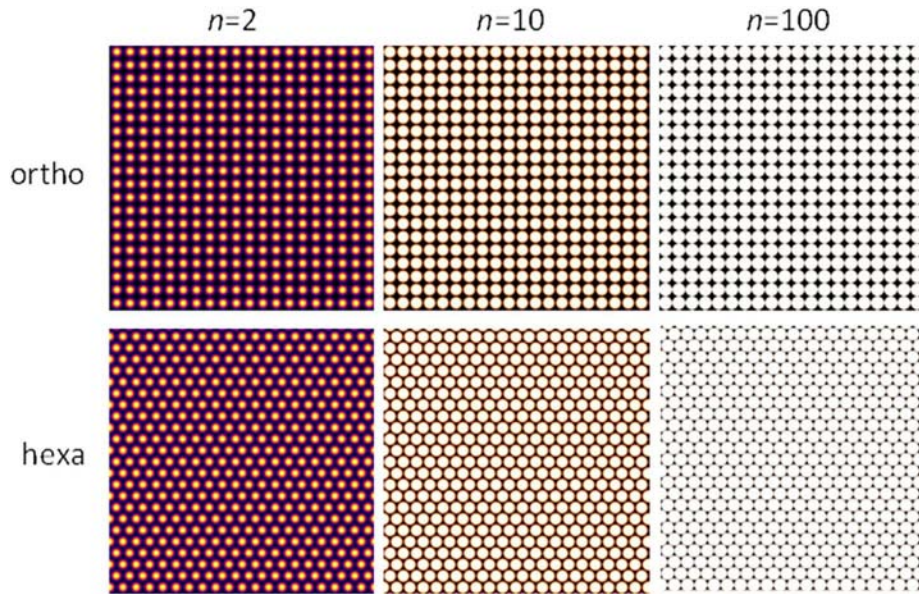
Fig. 2. Surface sampling on regular orthogonal (::) and hexagonal (∴) ablation grids by round beam profiles via compounding of ablation spots given in Fig. 1.
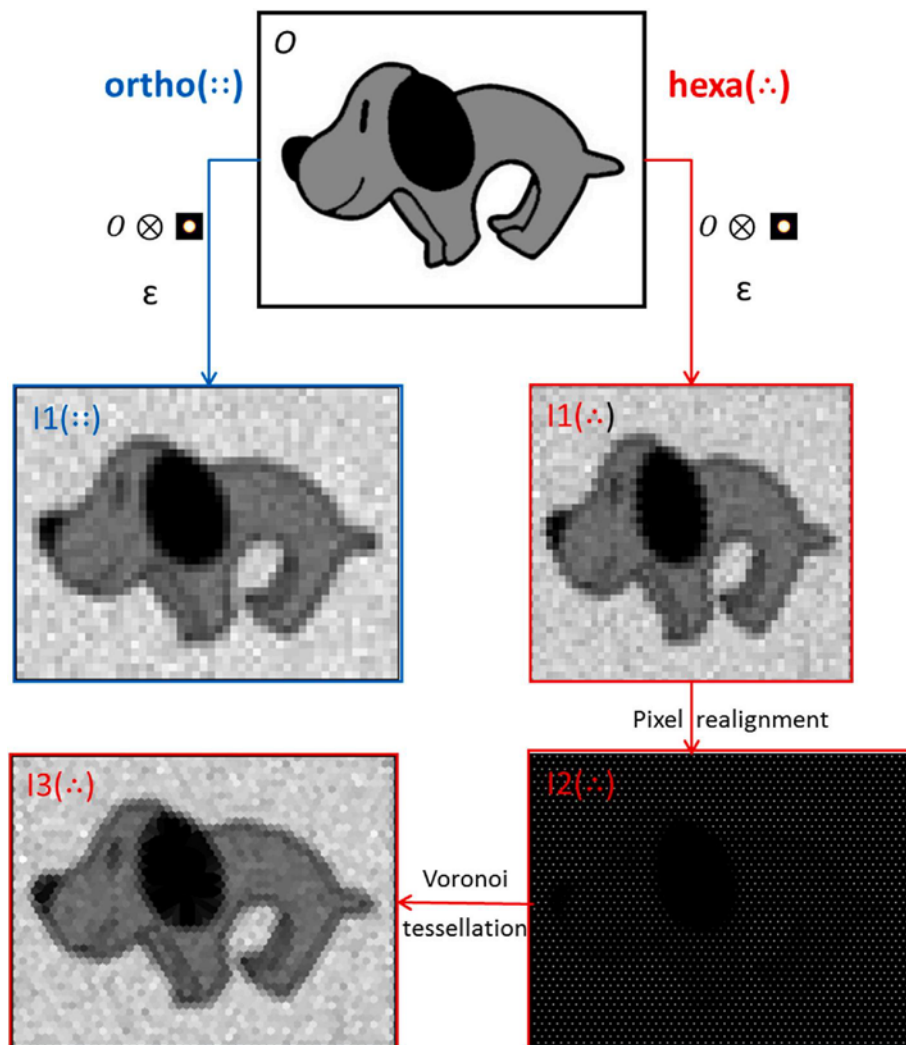

Fig. 3. Workflow associated with virtual LA-ICP-MS mapping of an object O with a round beam profile on an orthogonal (::) and hexagonal (∴) grid, respectively, yielding the images $I1$(::) and $I1$(∴) after applying/adding Poisson/Flicker noise ϵ; after positional realignment (staggering/interleaving), image $I2$(∴) is converted into a hexagonal image $I3$(∴) (in Cartesian coordinates). Due to upscaling and realignment, image $I2$(∴) is ca. 6 times larger (linear) than images $I3$(∴) and $I1$(::).

that the layout of round ablation spots on regular orthogonal (∷) and hexagonal (∴) grids, i.e., associated with the beam size selected and not the actual crater profile, is most efficient for a hexagonal grid and a beam profile as close as possible to a flat-top beam profile ($n = 100$). In that configuration the volume sampled for the same area is 2.6 times as large as sampling by a Gaussian beam profile ($n = 2$). We may bring the ablation spots closer together in case we are not dealing with flat-top beam profiles to more representatively sample the surface and get a smoother post-ablation surface, although we will mostly focus on the generic effect of ablation grid contraction associated with enhanced image quality due to increased pixel density.

Ablation grid coordinates (=ablation centers) for 2D-oversampling are directly associated with the contraction factors k (∷) and k (∴) via the effective ablation spot size $2\omega_0$ (=side length and diameter, respectively). The orthogonal ablation grid is given by

$$[2 \times g \times k(∷) \times \omega_0, 2 \times h \times k(∷) \times \omega_0 \,](\text{all rows}) \qquad (4)$$

where g and h are positive integers ($\mathbb{Z}^+$) associated with laser spot indexing in the ablation matrix. The hexagonal ablation grid with co-ordinates for the staggered/interleaved rows a and b is given by [23–25]

$$\left[2 \times g \times k(∴) \times \omega_0, 2 \times h \times \sqrt{3} \times k(∴) \times \omega_0 \right] \text{(row a)} \qquad (5a)$$

and

$$\left[(2 \times g + 1) \times k(∴) \times \omega_0, (2 \times h + 1) \times \sqrt{3} \times k(∴) \times \omega_0 \right) \right] \text{(row b)} \qquad (5b)$$

By 2D-oversampling via ablation grid contraction, i.e., $k(∷)<1$ and k (∴)<1, not only the post-ablation surface roughness and the depth of ablation are affected, but also the image quality in single pulse LA-ICP-MS mapping on orthogonal and hexagonal ablation grids as will be demonstrated below.

2.3. Virtual LA-ICP-MS mapping protocols

A theoretical base for the simulation of 2D sub-pixel single pulse LA-ICP-MS mapping on orthogonal and hexagonal grids as a function of the beam profile requires the development of numerical protocols for virtual mapping.

The flowchart in Fig. 3 shows the use of computational protocols for the simulation of the virtual LA-ICP-MS mapping procedure based on discrete convolution of an object O with a point spread function associated with a round crater profile to yield an image $I1(∷)$ or an image $I1$ (∴), using sampling on an orthogonal or a hexagonal grid, respectively, and applying/adding noise ϵ [8]. The noise is made up of Flicker noise (=$q \times P$, i.e., noise proportional to the number of counts P per pixel, where $0 < q < 1$) and Poisson noise (=$\sqrt{P}$, i.e., noise associated with counting statistics). It can be seen that image $I1(∴)$ is significantly shrunk in the horizontal direction since hexagonally sampled pixels are stored and displayed in regular matrix form. By positionally realigning the pixels into the correct staggered/interleaved fashion, associated with the hexagonal ablation grid, image $I2(∴)$ is obtained. This transformation requires that the matrix is sufficiently upscaled by introducing zeros around each data point according to the hexagonal layout, followed by Voronoi tessellation [26] to produce image $I3(∴)$, showing hexagonal pixels in a Cartesian coordinate system. Simulations were performed in MatLab R2020a (MathWorks), and for visualization of the data, Origin software (Origin 2018, OriginLab Corporation, North-ampton, MA) and ImageJ 1.49 [27] were used. An online app was created based on the above computational methodology in MatLab to study the effects of local concentration, instrumental sensitivity/noise, laser beam size/profile, orthogonal or hexagonal ablation grid, and contraction of the ablation grid on image map quality (spatial resolution and signal-to-noise ratio) by virtual LA-ICP-MS mapping of phantoms.

3. Results and discussion

3.1. Simulating image quality enhancement through contraction of orthogonal and hexagonal ablation grids in 2D single pulse LA-ICP-MS mapping

Via sub-pixel 2D convolution modeling on phantoms (high-resolution Vermeer image, chirp resolution target, and contrast-detail diagram; Fig. 4), using kernels associated with round ablation craters, the effects of 2D oversampling on image quality were assessed as a function of the beam profile, sampling grid, concentration, sensitivity, and noise. Via the online app (https://laicpms-apps.ki.si/webapps/home/; see SI-1 for app functionality), which incorporates mentioned phantoms, we can quickly learn how orthogonal and hexagonal sampling affects the image quality, whereas more detailed information can be gleaned from the mapping of chirp resolution target and contrast-detail (CD) diagrams, revealing specifics on spatial resolution and recognition of detail in a noisy background, respectively.

3.2. Visual acuity related to orthogonal and hexagonal sampling

To show the intricacies of orthogonal and hexagonal sampling, the cropped, high-resolution red, green and blue images in Fig. 4A (dimensions, 750×750 μm^2) were subjected to virtual LA-ICP-MS mapping with a 12-μm round super-Gaussian beam profile ($n = 10$), without the addition of noise, and contraction factors of 1, 0.5, and $0.3\bar{3}$. As no noise was introduced, the individual RGB channels could be treated identically in the simulation before recombining them in a color image again. As expected, the simulations in Fig. 5 show that the hexagonal maps look more natural than the orthogonal maps due to better representation of curves (caused by higher symmetry, higher sampling efficiency, equidistance, greater angular resolution, less aliasing effect, and consistent connectivity), but also its resemblance with the arrangement of photoreceptors in the human eye [16]. It is evident that due to a higher pixel density the 2D-oversampled images have a higher image quality than the non-oversampled images. To study the effect of noise on the image quality, the app performs these simulations on the grayscale image in Fig. 4A only. For retrieval of more specific information such as spatial resolution and recognition of details in the noise, specific phantoms (Fig. 4B and C) were used.

3.3. Spatial resolution

The spatial resolution of a system is mostly studied by measuring the modulation transfer function (MTF), based on imaging of a periodic grating (linear bar pattern, star bar pattern (slanted) knife edge, etc.), [28]. These procedures measure how the contrast changes as a function of the spatial periodicity Λ_m or spatial frequency f_m of features m in an image. If the image is not sampled finely enough to record all spatial frequencies, aliasing will occur and the spatial resolution, and thus image quality, is compromised. In practice one wants to sample the features m with a sampling frequency f_s of at least $2f_m$ or a sampling periodicity Λ_s of at most $\Lambda_m/2$, denoted as the Nyquist frequency or the Nyquist periodicity, respectively, to resolve the finest features m. 2D-oversampling ($f_s > 2f_m$ or $\Lambda_s < \Lambda_m/2$) minimizes aliasing and increases the spatial resolution as illustrated in Fig. 6.

The chirp resolution target is a special case of a periodic grating denoted by lines of different periods which vary exponentially with spatial position [19]. In this case, 50 single bars, having a period ranging between 166 and 15 μm and spanning a frequency range between 0.0060 and 0.0667 μm^{-1}. Fig. 6 shows the virtual ablation of this target as a function of the beam profile (n) and contraction factor ($k(∷)$ or $k(∴)$) for a 24-μm round laser beam. Distorted oscillating chirp signals after LA are a clear indication of aliasing as can be seen from ablation on non-contracted orthogonal ablation grids (k (∷) $= 1$) by yielding serious
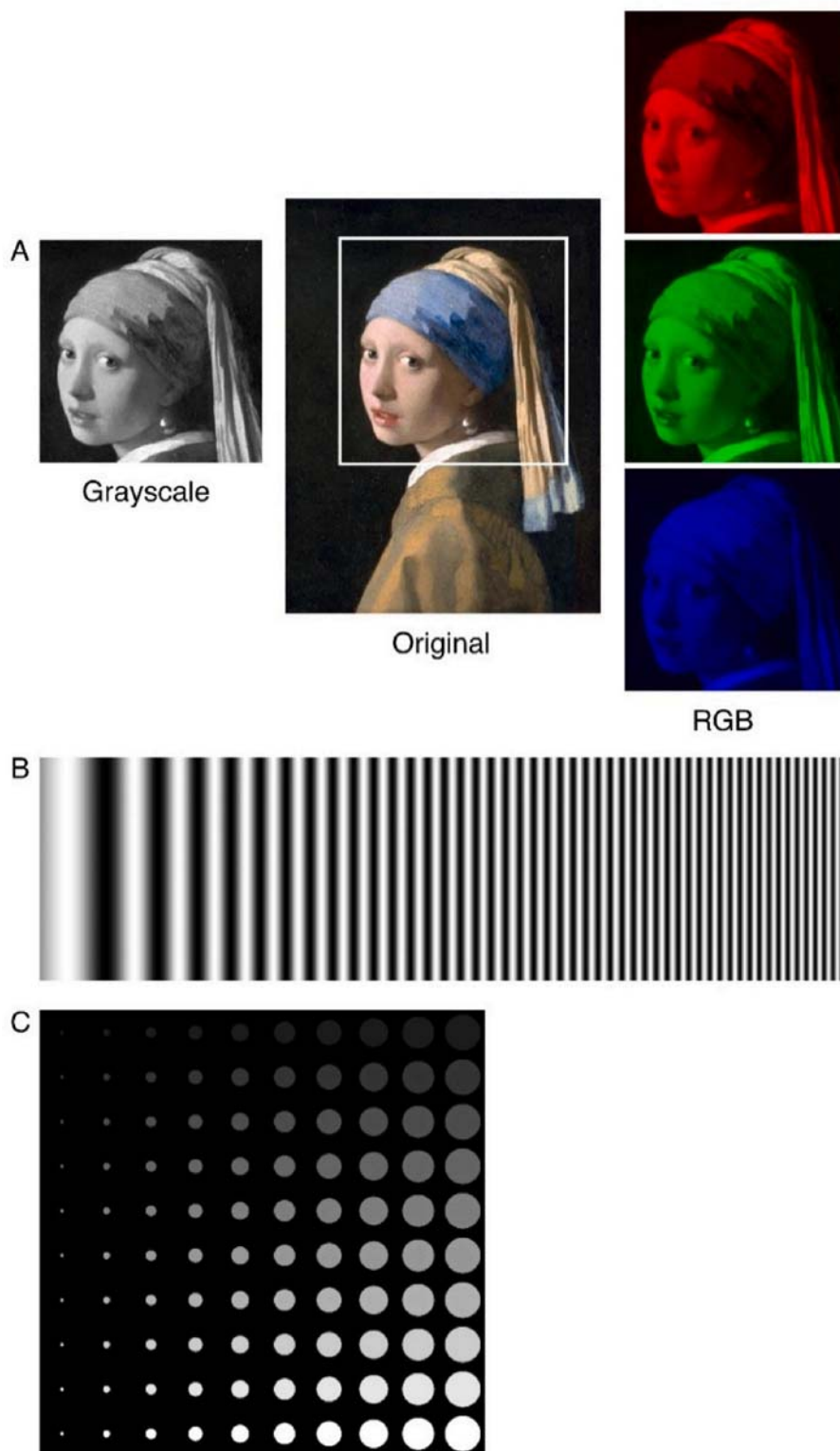
Fig. 4. Phantoms used in virtual LA-ICP-MS mapping: A) Johannes Vermeer image (ca. 1665), "Girl with a Pearl Earring" (10,000 × 8,443, Wikimedia Commons), cropped and resized to 3,000 × 3,000 pixels), followed by conversion to grayscale [left] and extraction of the RGB channels [right], B) chirp resolution target (10,000 × 2,000 pixels), and C) contrast-detail (CD) diagram (3,000 × 3,000 pixels); in all images, the pixel dimensions were 0.25 × 0.25 μm^2.

aliasing artifacts for all beam profiles, whereas at $k(::) = 0.5$ they are reduced and at $k(::) = 0.3\overline{3}$ they have mostly disappeared. Sampling on a hexagonal grid delivers in all instances a better resolution than sampling on an orthogonal grid, whereas it is evident that for lower k (::) and k (∴) factors in general a better spatial resolution is obtained as visible from

less converging oscillating patterns. Also, the beam profile affects the spatial resolution as can be seen from the hexagonal mapping of the chirp resolution target at $k(∴) = 0.3\overline{3}$, where the Gaussian beam converges the least, inferring that the lower the super-Gaussian order, the higher the spatial resolution. However, as 2D-oversampling increases
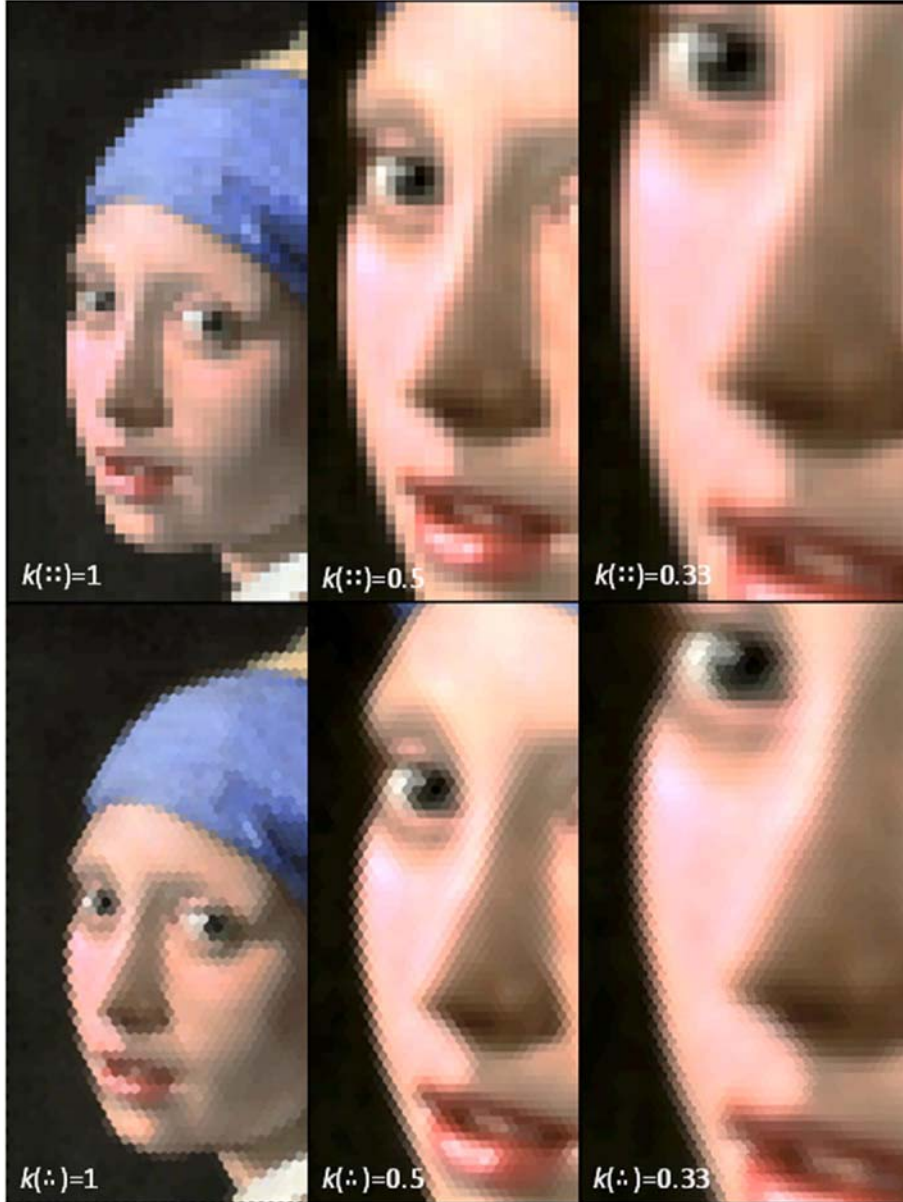
Fig. 5. Recombined red, green and blue images of the Johannes Vermeer image (Fig. 4A) after virtual LA-ICP-MS mapping via orthogonal (top row) or hexagonal (bottom row) sampling on ablation grids with contraction factors $k(::)$ and $k(\therefore)$ of 1, 0.5 and 0.33 using a round super-Gaussian beam profile ($n = 10$) without the introduction of noise. The oversampled output was zoomed in two times ($k(::) = k(\therefore) = 0.5$) or three times ($k(::)=0.3\overline{3}$) times so that it matched the pixel size of the non-oversampled output ($k(::) = k(\therefore) = 1$).

the analysis time in single pulse LA-ICP-MS, one may limit oversampling to contraction factors $k(::)$ and k $(\therefore)$ of $0.3\overline{3}$, as studies on pixelated-imager systems have shown that only negligible image quality improvement can be expected for lower contraction factors [29,30]. As noise influences the precision in the construction of the MTF, noise was not applied in the above experiments. However, as the spatial resolution is affected by noise [31,32], additional simulations were performed on CD diagrams to investigate how Flicker and Poisson noise alter the detectability of details in images.

3.4. Contrast and detail

Fundamental differences exist between imaging systems with high-contrast and low-contrast resolution. In general, the high-contrast resolution is limited by the intrinsic blurring of the imaging system, whereas at low contrast, objects (even very large objects) may not be discernible because the signal of the object is not distinguishable from the noise in the region containing the object. A simple way to illustrate the influence of noise on spatial resolution is by using the Rose model [33] that calculates the ability to detect an object based on the

contrast-to-noise ratio (*CNR*), associated with the object signal and the background noise using a so-called contrast-detail (CD) diagram (Fig. 4C). This CD diagram consists of 10 rows of 10 spots, each row having its contrast *C* defined by

$$C = (S_0 - S_{BG}) \, / \, (S_0 + S_{BG}) \tag{6}$$

where S_O and S_{BG} denote the number of counts in object and background, respectively; from top to bottom the rows gradually decrease in contrast from $0.3\overline{3}$ to 0.818, whereas from left to right the spots increase in diameter from 6 to 60 μm. Upon single pulse LA-ICP-MS mapping, Flicker and Poisson noise will be introduced, and as a result, the contrast will decrease, depending on the concentration levels and instrumental sensitivity/noise. As most noise at low count numbers is associated with Poisson noise, according to the Rose criterion an object is distinguishable from the background when the effective CNR_{eff} denoted by

$$CNR_{eff} = \sqrt{N_{pixel}} \times (S_O - S_{BG})/\sigma_{BG} \tag{7}$$

exceeds a value of 3–5 [34] for spots comprising *N* pixels, with σ_{BG} denoting the standard deviation of the background. We used a value of 7
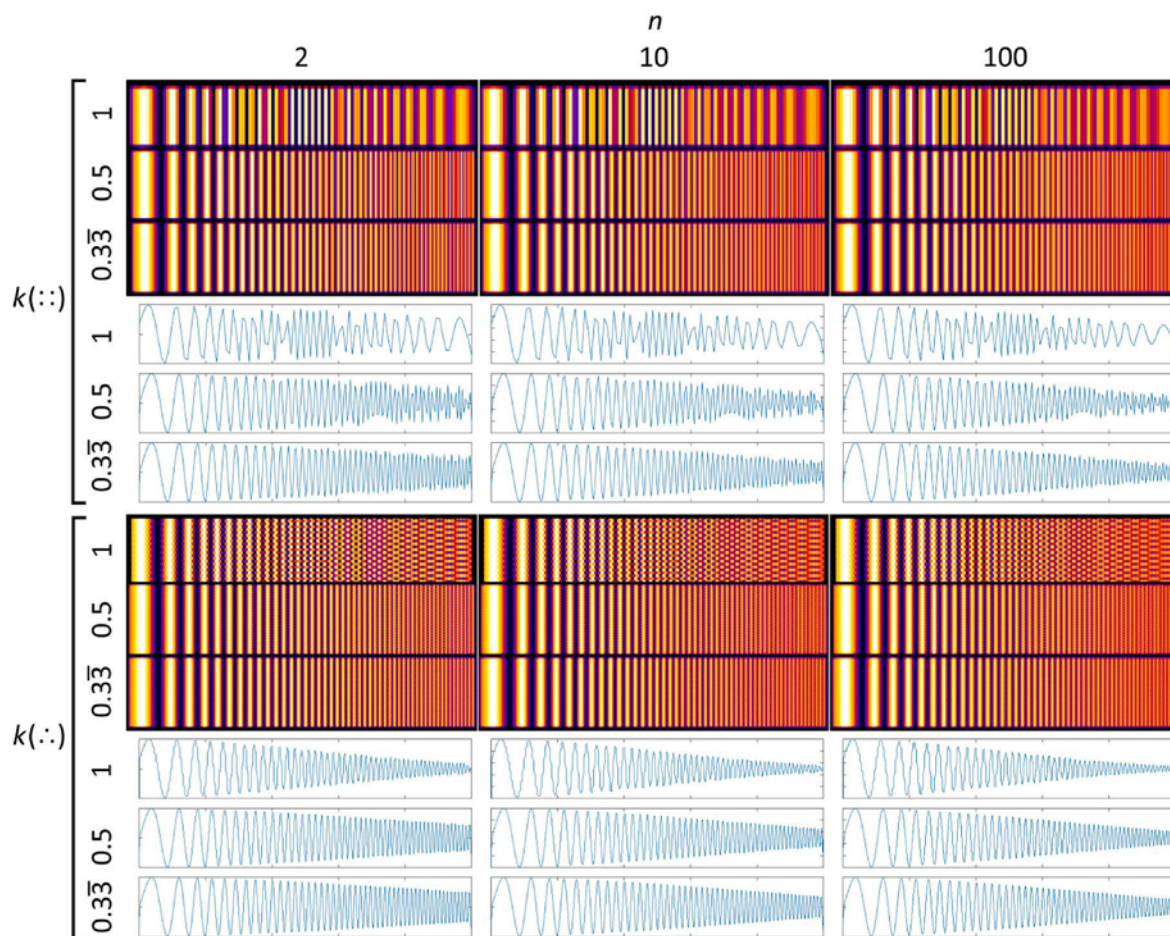
Fig. 6. Virtually mapped 2,500 × 500 μm² chirp resolution target (Fig. 4B) based on orthogonal (::) and hexagonal (∴) sampling applying contraction factors k(::) and k(∴) of 1, 0.5 and 0.3$\overline{3}$, and using a round beam size of 24 μm with profiles associated with super-Gaussian orders n of 2, 10, and 100 (no noise was introduced in this experiment).

for CNR_{eff} as the Rose criterion where lower and higher values indicate non-detectability and detectability, respectively.

To demonstrate the correctness of this Rose criterion, the CD diagram was subjected to virtual LA-ICP-MS mapping with a round 12-μm beam. Differently contracted orthogonal and hexagonal grids (contraction factors of 1, 0.5, and 0.3$\overline{3}$), and the use of various beam profiles (Gaussian orders of 2, 10, and 100) under very low-contrast conditions, led to the output presented in Fig. S2 (SI-2). From the blue traces, representing the Rose criterion for a CNR_{eff} value of 7, it is clear that this criterion defines detectability truthfully. As the pixel density increases with decreasing contraction factor, to compare the oversampled output with the non-oversampled output, the oversampled output maps (for contraction factors of 0.5 and 0.3$\overline{3}$) were resized to the size of the non-oversampled output maps (contraction factor of 1). By resizing via averaging of respective 2 × 2 or 3 × 3 pixels, in essence we reduce the noise by a factor of two or three (1/k(::) or 1/k(∴)), which results in better detectability as obvious from the Rose criterion traces in Fig. 7 (extracted from Fig. S2 (SI-2) and overlaid on the original CD diagram). We can also see that in most instances hexagonal mapping yields (marginally) better detail of objects in a noisy background; only for a laser beam approaching a flat-top profile (n = 100) without oversampling (k(::) = k(∴) = 1) the hexagonal ablation grid generates significantly more detail than the orthogonal ablation grid.

3.5. Experimental proof of concept

The fact that commercial, hexagonal stages are currently not avail-

able for LA-ICP-MS mapping makes it difficult to experimentally proof the benefits of hexagons compared to squares. The reason is that conventional orthogonal stages are not accurate enough to lay out a hexagonal ablation grid at the microscale level due to the micrometer-based step size and the fact that staggered/interleaved hexagons have ablation grid points spaced "one-beam-size" apart in one direction and "one-beam-size × 0.5 × $\sqrt{3}$" in the other direction. We could confirmed our modeling findings experimentally by using an inkjet-printed cyan color macroscale resolution target (Fig. S3A, SI-3) and employing a large beam size (150 μm) to map Cu in the cyan ink (Fig. S3B, SI-3). This approach mitigates the inaccuracy of the orthogonal stages for hexagonal mapping, and shows that for contraction factors k(::) and k(∴) of 1, hexagonal sampling indeed results in higher spatial resolution and hence better image quality (Fig. S3C, SI-3).

4. Conclusions

The online app (https://laicpms-apps.ki.si/webapps/home/), using various phantoms, makes it possible to quickly simulate the effect of 2D-oversampling on orthogonal and hexagonal ablation grids in LA-ICP-MS mapping with respect to image quality, taking into account the spatial resolution and noise. Also other laser-based mass spec imaging techniques such as matrix-assisted laser desorption/ionization (MALDI), laser desorption/ionization droplet delivery - mass spectrometry (LDIDD-MS), laser ablation electrospray ionization - MS (LAESI-MS), etc. may benefit from this approach to optimize the image quality related to their specific operational parameters. Computational
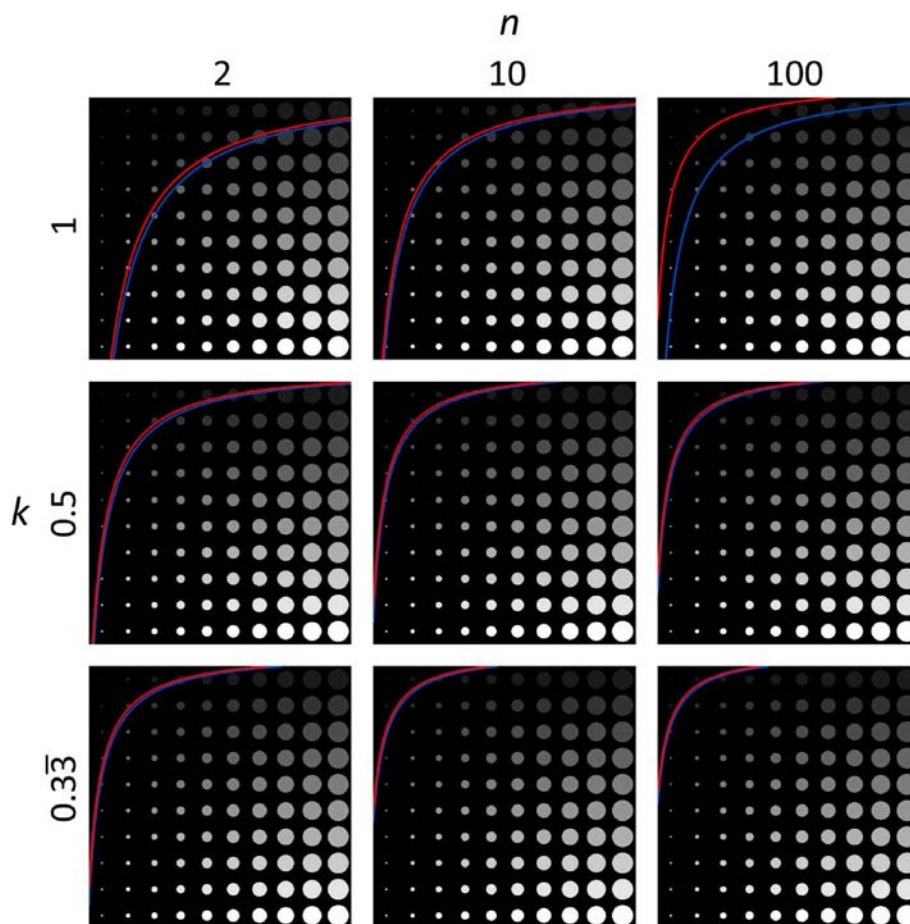
Fig. 7. Detectability of virtually ablated CD diagrams according to the Rose criterion; shown are traces representing the Rose criterion for a CNR_{eff} value of 7 (see Eq. (7)) for orthogonal (blue trace) and hexagonal (red trace) sampling, respectively. The 750×750 μm^2 CD diagram (Fig. 4C) was sampled with a round beam size of 12 μm assuming a maximum concentration of 2 ppm, a background concentration of 0.2 ppm, 5% Flicker noise, and a sensitivity of 0.06 ct $ppm^{-1} \cdot \mu m^{-3}$ per pulse.

protocols are based on discrete convolution with a kernel related to the 3D ablation crater topography, followed by applying/adding Poisson/ Flicker noise based on the local concentration and instrumental sensitivity. It was shown that through oversampling, aliasing and phase distortion can be avoided and signal-to-noise ratios enhanced, thereby improving the spatial resolution and detail recognition, respectively. Sampling on a hexagonal grid yielded under all mapping conditions a better image quality although differences were most pronounced for non-oversampled flat-top crater topographies. Although hexagonal mapping in a Cartesian coordinate system is experimentally possible for 2D LA-ICP-MS mapping on the macroscale, the stages and actuators driving it lack precision for true hexagonal sampling. This would be an avenue for future work by developing stages that operate in hexagonal fashion, and utilize its many potential advantages (more efficient sampling, consistent connectivity, equidistant neighboring pixels, greater angular resolution, and higher circular symmetry). Via geometrical modelling [35], the ablation grid can then be further optimized to generate the smoothest possible post-ablation surface and facilitate repetitive surface sampling or targeting of a certain ablation depth.

Credit author statement

Johannes T. van Elteren: Conceptualization, Methodology, Writing-Original Draft. Dino Metarapi: Visualization, Software, Writing-Reviewing & Editing.

Declaration of competing interest

The authors declare that they have no known competing financial interests or personal relationships that could have appeared to influence the work reported in this paper.

Data availability

Data will be made available on request.

Acknowledgments

Appendix A. Supplementary data

Supplementary data to this article can be found online at https://doi.org/10.1016/j.talanta.2023.124699.

References

[1] S.J.M. Van Malderen, A.J. Managh, B.L. Sharp, F. Vanhaecke, Recent developments in the design of rapid response cells for laser ablation-inductively coupled plasma-mass spectrometry and their impact on bioimaging applications, J. Anal. At. Spectrom. 31 (2016) 423–439, https://doi.org/10.1039/C5JA00430F.

[2] T. Van Acker, S.J.M. Van Malderen, T. Van Helden, C. Stremtan, M. Šala, J.T. Van Elteren, F. Vanhaecke, Analytical figures of merit of a low-dispersion aerosol transport system for high-throughput LA-ICP-MS analysis, J. Anal. At. Spectrom. 36 (2021) 1201–1209, https://doi.org/10.1039/d1ja00110h.

[3] A. Gundlach-Graham, M. Burger, S. Allner, G. Schwarz, H.A.O. Wang, L. Gyr, D. Grolimund, B. Hattendorf, D. Günther, High-speed, high-resolution, multi-elemental LA-ICP-TOFMS imaging: Part I. Instrumentation and two-dimensional imaging of geological samples, Anal. Chem. 87 (2015) 8250–8258, https://doi.org/10.1021/acs.analchem.5b01196.

[4] S.J.M. Van Malderen, T. Van Acker, B. Laforce, M. De Bruyne, R. de Rycke, T. Asaoka, L. Vincze, F. Vanhaecke, Three-dimensional reconstruction of the distribution of elemental tags in single cells using laser ablation ICP-mass spectrometry via registration approaches, Anal. Bioanal. Chem. 411 (2019) 4849–4859, https://doi.org/10.1007/s00216-019-01677-6.

[5] S.J.M. Van Malderen, T. Van Acker, F. Vanhaecke, Sub-micrometer nanosecond LA-ICP-MS imaging at pixel acquisition rates above 250 Hz via a low-dispersion setup, Anal. Chem. 92 (2020) 5756–5764, https://doi.org/10.1021/acs.analchem.9b05056.

[6] O.B. Bauer, O. Hachmöller, O. Borovinskaya, M. Sperling, H.J. Schurek, G. Ciaromboli, U. Karst, LA-ICP-TOF-MS for rapid, all-elemental and quantitative bioimaging, isotopic analysis and the investigation of plasma processes, J. Anal. At. Spectrom. 34 (2019) 694–701, https://doi.org/10.1039/c8ja00288f.

[7] A. Limbeck, P. Galler, M. Bonta, G. Bauer, W. Nischkauer, F. Vanhaecke, Recent advances in quantitative LA-ICP-MS analysis: challenges and solutions in the life sciences and environmental chemistry, Anal. Bioanal. Chem. 407 (2015) 6593–6617, https://doi.org/10.1007/s00216-015-8858-0.

[8] J.T. van Elteren, M. Šala, D. Metarapi, Comparison of single pulse, multiple dosage, and 2D oversampling/deconvolution LA-ICPMS strategies for mapping of (ultra) low-concentration samples, Talanta 235 (2021), https://doi.org/10.1016/j.talanta.2021.122785.

[9] M. Šala, V.S. Šelih, C.C. Stremtan, T. Tămaş, J.T. van Elteren, Implications of laser shot dosage on image quality in LA-ICP-QMS imaging, J. Anal. At. Spectrom. 36 (2021) 75–79, https://doi.org/10.1039/d0ja00381f.

[10] J.T. van Elteren, V.S. Šelih, M. Šala, Insights into the selection of 2D LA-ICP-MS (multi)elemental mapping conditions, J. Anal. At. Spectrom. 34 (2019) 1919–1931, https://doi.org/10.1039/c9ja00166b.

[11] J.T. van Elteren, V.S. Šelih, M. Šala, S.J.M. Van Malderen, F. Vanhaecke, Imaging artifacts in continuous scanning 2D LA-ICP-MS imaging due to non-synchronization issues, Anal. Chem. 90 (2018) 2896–2901, https://doi.org/10.1021/acs.analchem.7b05134.

[12] S.J.M. Van Malderen, J.T. van Elteren, V.S. Šelih, F. Vanhaecke, Considerations on data acquisition with scanning mass spectrometers in laser ablation – inductively Coupled Plasma-mass spectrometry with low-dispersion interfaces, Spectrochim. Acta Part B At. Spectrosc. 140 (2017) 29–34, https://doi.org/10.1016/j.sab.2017.11.007.

[13] O.B. Bauer, O. Hachmöller, O. Borovinskaya, M. Sperling, H.J. Schurek, G. Ciaromboli, U. Karst, LA-ICP-TOF-MS for rapid, all-elemental and quantitative bioimaging, isotopic analysis and the investigation of plasma processes, J. Anal. At. Spectrom. 34 (2019) 694–701, https://doi.org/10.1039/c8ja00288f.

[14] M. Wiegelmann, K. Dreisewerd, J. Soltwisch, Influence of the laser spot size, focal beam profile, and tissue type on the lipid signals obtained by MALDI-MS imaging in oversampling mode, J. Am. Soc. Mass Spectrom. 27 (2016) 1952–1964, https://doi.org/10.1007/s13361-016-1477-y.

[15] S.J.M. Van Malderen, J.T. van Elteren, F. Vanhaecke, Submicrometer imaging by laser ablation-inductively coupled plasma mass spectrometry via signal and image deconvolution approaches, Anal. Chem. 87 (2015) 6125–6132, https://doi.org/10.1021/acs.analchem.5b00700.

[16] I. Singh, A. Oberoi, Comparison between square pixel structure and hexagonal pixel structure in digital image processing, Int. J. Comput. Sci. Trends Technol. 3 (2015) 176–181.

[17] J.D. Mollon, J.K. Bowmaker, The spatial arrangement of cones in the primate fovea, Nature 360 (1992) 677–679.

[18] C.A. Curcio, K.R. Sloan, R.E. Kalina, A.E. Hendrickson, 902920402_Ftp.Pdf, J. Comp. Neurol. 292 (1990) 497–523.

[19] A. González-López, Chirp phantom for MTF calculations. A study of its precision in noisy environments, Phys. Med. 48 (2018) 65–71, https://doi.org/10.1016/j.ejmp.2018.04.001.

[20] J.T. van Elteren, F. Vanhaecke, Angular resolution dependency in 2D LA-ICP-MS mapping – the case for low-dispersion laser ablation cells, J. Anal. At. Spectrom. 31 (2016) 1998–2004, https://doi.org/10.1039/C6JA00234J.

[21] S. Verma, J. Hesser, S. Arba-Mosquera, Optimum laser beam characteristics for achieving smoother ablations in laser vision correction, Investig. Ophthalmol. Vis. Sci. 58 (2017) 2021–2037, https://doi.org/10.1167/iovs.16-21025.

[22] C. Wei, Y. Ma, Y. Han, Y. Zhang, L. Yang, X. Chen, Study on femtosecond laser processing characteristics of nano-crystalline CVD diamond coating, Appl. Sci. 9 (2019), https://doi.org/10.3390/app9204273.

[23] W. Snyder, H. Qi, W. Sander, A coordinate system for hexagonal pixels, Proc. Int. Soc. Opt. Eng. 3661 (1999) 716–727.

[24] J.W. Van Roessel, Conversion of cartesian coordinates from and to generalized balanced ternary addresses, Photogramm. Eng. Rem. Sens. 54 (1988) 1565–1570.

[25] S. Fadaei, A. Rashno, A framework for hexagonal image processing using hexagonal pixel-perfect approximations in subpixel resolution, IEEE Trans. Image Process. 30 (2021) 4555–4570, https://doi.org/10.1109/TIP.2021.3073328.

[26] Q. Du, V. Faber, M. Gunzburger, Centroidal Voronoi tessellations: applications and algorithms, SIAM Rev. 41 (1999) 637–676, https://doi.org/10.1137/S0036144599352836.

[27] C.A. Schneider, W.S. Rasband, K.W. Eliceiri, NIH Image to ImageJ: 25 years of image analysis, Nat. Methods 9 (2012) 671–675, https://doi.org/10.1038/nmeth.2089.

[28] A. González-López, Effect of noise on MTF calculations using different phantoms, Med. Phys. 45 (2018) 1889–1898, https://doi.org/10.1002/mp.12847.

[29] O. Hadar, G.D. Boreman, Analysis of Oversampling Requirements in Infrared Scene Projectors, Infrared Spaceborne Remote Sens. 3122 (1997) 286–294.

[30] O. Hadar, G.D. Boreman, Oversampling requirements for pixelated-imager systems, Opt. Eng. 38 (1999) 782, https://doi.org/10.1117/1.602044.

[31] M. Senoner, T. Wirth, W.E.S. Unger, Imaging surface analysis: lateral resolution and its relation to contrast and noise, J. Anal. At. Spectrom. 25 (2010) 1440–1452, https://doi.org/10.1039/c004323k.

[32] J.T. van Elteren, A. Izmer, V.S. Šelih, F. Vanhaecke, Novel image metrics for retrieval of the lateral resolution in line scan-based 2D imaging via an experimental-modeling approach, Anal. Chem. 88 (2016) 7413–7420, https://doi.org/10.1021/acs.analchem.6b02052.

[33] R.E. Hendrick, Spatial Resolution in Magnetic Resonance Imaging, 2008, https://doi.org/10.1007/978-0-387-73507-8_3.

[34] S.R. Cherry, J.A. Sorenson, M.E. Phelps, Physics in Nuclear Medicine, Elsevier Health Sciences, 2012.

[35] J.T. van Elteren, D. Metarapi, K. Mervič, M. Šala, Exploring the benefits of ablation grid adaptation in 2D/3D LA-ICP-MS mapping through geometrical modeling, Anal. Chem., accepted for publication.